Energy & Environmental Science

ROYAL SOCIETY OF CHEMISTRY

PAPER

View Article Online
View Journal | View Issue

Cite this: *Energy Environ. Sci.*, 2024, **17**, 1497

Highly stable manganese oxide cathode material enabled by Grotthuss topochemistry for aqueous zinc ion batteries†

Fangjia Zhao, [a] Jianwei Li,[b] Arunabhiram Chutia, [c] Longxiang Liu,[a] Liqun Kang,[d] Feili Lai, [e] Haobo Dong,[a] Xuan Gao,[a] Yeshu Tan,[a] Tianxi Liu,[f] Ivan P. Parkin *[a] and Guanjie He *[a]

Received 2nd December 2023,
Accepted 15th January 2024

DOI: 10.1039/d3ee04161a

rsc.li/ees

The design and synthesis of manganese oxide-based materials with high-rate performance and long cycle life is a major challenge for aqueous zinc-ion batteries (AZIBs). This research reports the presence of a synergistic collaboration between vacancies, lattice water and nickel ions on enhancing the hydrated protons hopping *via* the Grotthuss mechanism for high-performance zinc ion batteries. The Grotthuss mechanism allows for the efficient transfer of a proton charge without the actual movement of the molecule over long distances, resulting in high ionic conductivity. $NiMn_3O_7{\cdot}3H_2O$ achieves a capacity of 318 mA h g^{-1} under 200 mA g^{-1} and 121 mA h g^{-1} under 5 A g^{-1} with a retention of 91% after 4000 cycles. The relationship between the remarkable performance and Grotthuss topochemistry is investigated using techniques including synchrotron X-ray absorption spectroscopy and density functional theory. Protons prefer to bond with O^{2-} ions on the Mn–O layer, and proton transfer is favoured in the presence of vacancies. The continuous hopping of protons within the host material induces periodic, temporary local structural changes in the lattice. This dynamic behaviour alters the energy barriers for ions intercalation and deintercalation. Nickel ions facilitate the ongoing mobility of hydrated protons *via* Grotthuss hopping by preserving the system's electrical neutrality, which counterbalances the dynamic changes caused by proton migration. This study provides insight into the Grotthuss conduction mechanism for the development of high-performance cathode materials in AZIBs.

Broader context

As an electrochemical energy storage system, zinc-ion batteries have attracted significant attention, benefiting from the low cost and abundant reserves of zinc. However, the practical utility of zinc-ion batteries is restricted by the limited performance of the cathode materials. Manganese oxide cathode materials have been extensively researched because of their comparatively high discharge plateau and satisfactory theoretical capacity. Although significant efforts have been undertaken to enhance the performance (lifespan and capacity) of manganese oxides, understanding the energy storage mechanism remains constrained. Notably, the hydrated proton collaborates with the zinc cation to complete the intercalation/deintercalation process, hence enhancing the battery's capacity. However, the mechanism of hydrated protons remains insufficiently understood. Here, we uncover the presence of a synergistic collaboration between vacancies and lattice water on the Grotthuss mechanism of hydrated protons. Experiments and computational studies have revealed that vacancies in the lattice serve as a driving force for proton hopping, while water molecules act as conduits for proton hopping during the Grotthuss process. Hydrated protons exhibit a tendency to migrate *via* vacancy sites with reduced barriers. This would enable the hydrated proton to move through the periodic variation of vacancies. Moreover, the stability of the cathode material is improved because nickel cations preserve the system's electrical neutrality, which counterbalances the dynamic changes caused by charge carriers' migration in the lattice. We use a controllable hydrothermal approach to generate abundant vacancies and improve the diffusion mechanism. As a result, the cathode material $NiMn_3O_7$ that has been developed demonstrates an improved energy storage mechanism.

[a] *Department of Chemistry, University College London, 20 Gordon Street, London WC1H 0AJ, UK. E-mail: i.p.parkin@ucl.ac.uk, g.he@ucl.ac.uk*
[b] *Key Laboratory of Comprehensive and Highly Efficient Utilization of Salt Lake Resources, Qinghai Province Key Laboratory of Resources and Chemistry of Salt Lakes, Qinghai Institute of Salt Lakes, Chinese Academy of Sciences, Xining, Qinghai 810008, P. R. China*
[c] *School of Chemistry, University of Lincoln, Brayford Pool, Lincoln, LN6 7TS, UK*
[d] *Max Planck Institute for Chemical Energy Conversion, Stiftstrasse 34-36, 45470 Mülheim an der Ruhr, Germany*
[e] *Department of Chemistry, KU Leuven Celestijnenlaan 200F, Leuven 3001, Belgium*
[f] *School of Chemical and Material Engineering, Jiangnan University, No. 1800, Lihu Avenue, Wuxi 214122, China*

† Electronic supplementary information (ESI) available: Experimental and computational details, and supplementary figures and tables. See DOI: https://doi.org/10.1039/d3ee04161a

Introduction

Driven by the practical need for safety and cost-effectiveness, aqueous zinc-ion batteries (AZIBs) have recently gained significant attention. MnO_2 has attracted extensive research due to its relatively high discharge plateau and lifespan. However, the development of manganese oxide cathode materials is hindered by their unsatisfactory lifespan at low current densities, which is attributed to the bivalency of the Zn^{2+} cation, *i.e.*, the strong electrostatic interaction between the Zn^{2+} cations and the host frameworks slows down its transport. The high desolvation energy of Zn^{2+} at the electrode–electrolyte interface, compared to its monovalent counterpart, imposes an extra energy penalty on its intercalation in manganese oxide. The relatively strong electrostatic repulsion between the charge carrier and manganese oxide during intercalation and deintercalation also limits ion transfer in AZIBs. Thus, enhancing the kinetics of charge carriers within manganese oxide materials is a crucial aspect of AZIBs cathode research.[1,2]

According to several prior studies, the Grotthuss mechanism is considered to be an efficient conductivity process because it implies the collective chain-like proton transfer, where the net charge, in principle, can be transported faster than a proton itself.[3–7] The Grotthuss mechanism provides more efficient proton transport because it does not require the mobility of entire molecules. The synergy between defect engineering and the Grotthuss mechanism could enhance the charge carrier kinetics (Fig. 1(a)). A recent study indicates that Grotthuss conduction can occur in defective Prussian blue analogues.[8] In this mechanism, a hydrogen atom hops between two hydrogen-bonded water molecules, displacing one of the molecule's existing H atoms and causing a cascade of identical displacements along the hydrogen-bonding network.[9] This motion is akin to Newton's cradle (Fig. 1(b)), with correlated local displacements leading to long-range transport of protons.[10,11] This allows for the fast, efficient transfer of protons without the need for a proton to travel the entire structure solely. The continuous hopping of protons across the host material can induce periodic but temporary, local structural changes in the lattice, simultaneously changing the energy barriers for zinc ion intercalation and deintercalation in the lattice, which optimise the diffusion pathways for zinc ions. Furthermore, the presence of manganese vacancies in the lattice not only serves as the low energy barrier pathways for proton hopping but also can serve as additional sites for both proton and zinc ion intercalation and increase the capacity of the battery. Defect engineering has been proven to be a facile strategy to modify the electronic structures of host materials and alter the energy barrier for charge carrier transfer.[12–16] The most prevalent cation vacancy in manganese oxides is Mn vacancy. By comparing the density of states of manganese oxide with and without vacancies, it has been proposed that introducing Mn vacancies into the manganese oxide framework can lead to an increase in the charge density at the Fermi level and can result in a lower surface energy barrier.[17] Furthermore, unlike the homogeneous charge distribution in typical manganese oxide, the electrons in defective manganese oxide congregate near the Mn vacancy. Defect-induced local structural

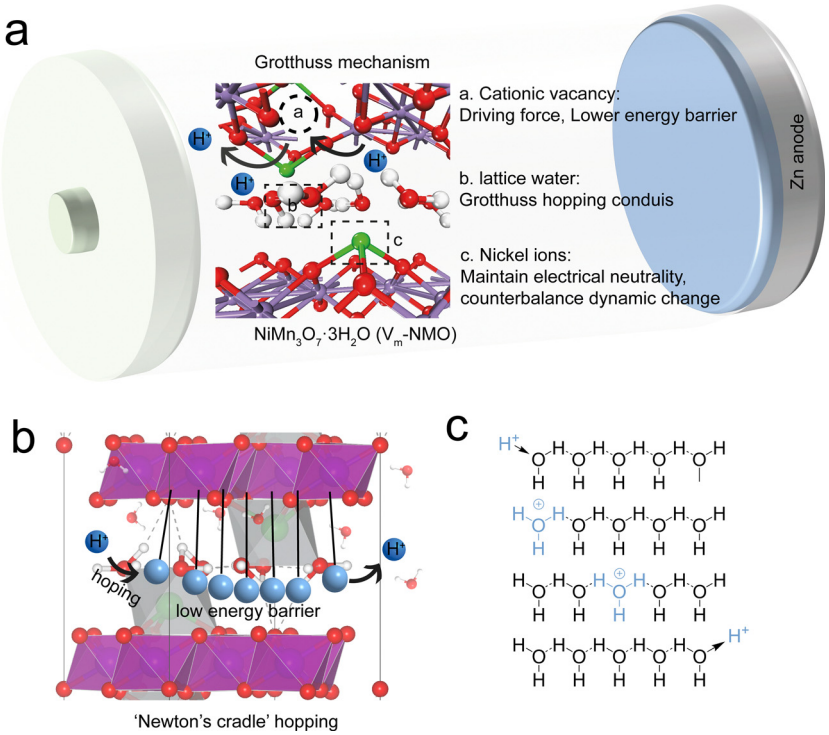

Fig. 1 (a) Hopping Grotthuss mechanism for proton conductivity. (b) Newton's cradle illustration of proton hopping Grotthuss mechanism in $NiMn_3O_7$ lattice. (c) Illustration of hydrated proton hopping *via* Grotthuss mechanism.

changes and charge redistribution can facilitate charge transfer and accommodate the volume changes associated with ion intercalation.

A strategic approach needs to be developed for achieving the Grotthuss mechanism in manganese oxide-based AZIBs. This approach should focus on two key aspects: (i) constructing a continuous hydrogen bond network in lattice to facilitate the proton migration from the electrolyte to cathode material interlayer space and (ii) mitigating the energy barrier for charge transfer within the host cathode material *via* defect engineering.[18–20] By effectively addressing these challenges, the efficient operation of AZIBs through the Grotthuss conduction mechanism can be realised, leading to improved energy storage performances.

This study presents a unique strategy to enhance the rate performance and long-term cycling stability of aqueous zinc ion batteries by utilising the Grotthuss mechanism in manganese oxide. A facile hydrothermal synthesis process was employed to prepare Ernie nickelite $NiMn_3O_7$. We found that the specific peak intensity and lattice structure in $NiMn_3O_7$ could be tailored by altering the synthesis conditions. The optimisation led to the formation of vacancies in the lattice. For convenience, the resulting samples are ascribed as V_m-NMO (with vacancy) and NMO (without vacancy). It was demonstrated that V_m-NMO can be used as highly reversible and high-capacity cathode materials for aqueous zinc ion batteries. The prepared cathode material V_m-NMO, containing abundant cation vacancies, exhibits an enhanced ion transfer and a high capacity of 318 mA h g^{-1} at a current density of 200 mA g^{-1}, along with a stable capacity of 121 mA h g^{-1} at 5 A g^{-1} and a capacity retention of 91% over 4000 cycles was achieved. Furthermore, the energy storage mechanism of the V_m-NMO cathode material was systematically investigated by combining synchrotron X-ray absorption spectroscopy with density functional theory (DFT) simulations. In aqueous electrolytes, protons react with water molecules, forming hydronium ions (H_3O^+). The numerous lattice water molecules within the host material create a continuous hydrogen bond network, which opens corridors for the migration of abundant water molecules from the electrolyte to the interlayer spaces in the layered manganese oxides. Our results indicate that protons prefer to bond with O^{2-} ions on the Mn–O layer rather than staying with water molecules. Additionally, energy barrier calculations for proton transfer with and without Mn^{4+} vacancies indicate that proton transfer is favoured in the presence of defects. Mn^{4+} vacancies are the driving force for proton hopping in the V_m-NMO systems. The continuous hopping of protons within the host material induces periodic, temporary local structural changes in the lattice. This dynamic behaviour alters the energy barriers for ion intercalation and deintercalation, optimising the diffusion pathways for zinc ions. Moreover, the presence of manganese vacancies in the lattice serves as low-energy barrier pathways for proton hopping and additional sites for proton and zinc ion intercalation, resulting in an increased battery capacity. This dynamic behaviour raises an interesting point regarding the Grotthuss-like mechanism on the Mn–O layer in V_m-NMO.

Results and discussion

Characterisation of the V_m-NMO and NMO cathode material structure

$NiMn_3O_7$ nanoparticles were synthesised using a facile hydrothermal synthesis method, and the V_m-NMO nanoparticle with vacancies was synthesised by optimising the synthesis parameter.[21] Detailed synthesis process is included in ESI.† To examine the impact of the synthesis parameter on the crystal structure. We conducted a series of experiments to investigate by varying the amount of synthesis precursors and temperature. The effects of different NH_4Cl adding amounts were examined in ESI,† Fig. S1. The synthesis experiment indicates that the optimal NH_4Cl concentration for promoting $NiMn_3O_7$ formation is 0.04 mol L^{-1}. Concentrations exceeding 0.4 mol L^{-1} result in a phase transition from $NiMn_3O_7$ to alpha-MnO_2. The impact of varied synthesis temperatures was studied in ESI,† Fig. S2. The XRD results show that the formation of vacancies in $NiMn_3O_7$ is highly sensitive to the temperature. The optimized $NiMn_3O_7$ synthesis temperature is 200 °C, lower temperature than 180 °C can lead to mixed phase products while temperature higher than 260 °C can lead to the product phase transition from $NiMn_3O_7$ to $NiMn_2O_4$. The X-ray diffraction (XRD) pattern of the as-prepared V_m-NMO and NMO (Fig. 2(a) and (b)) matched well with Ernie nickelite $NiMn_3O_7{\cdot}3H_2O$ (JCPDS: 46-1476), which belongs to hexagonal R^*(148) space group and has corresponding lattice constants of a = 7.5293(4) Å and c = 20.752(1) Å.[22] Defects and vacancies in the crystal structure of the material can alter the XRD pattern by modifying the spacing between the crystal planes. The main difference between V_m-NMO and NMO lies in (101), (012) and (003) crystal planes. The significant absence of (101) and (012) in the V_m-NMO lattice indicates lattice changes in the crystal structure, which can be due to preferred orientation or preferred crystal growth. Additionally, the intensity of the (003) lattice plane is significantly reduced, indicating disrupted long-range order of V_m-NMO and increased disorder of the lattice. The Mn atoms, which are octahedrally coordinated by six oxygen atoms, and form MnO_6 octahedra that connect along common edges to create a two-dimensional layer. The Mn_3O_7 layer is formed by periodically removing 1/7 of the Mn atoms in a triangular lattice, resulting in a maple-leaf-lattice (MLL) structure consisting of Mn^{4+} ions. The Mn_3O_7 layers are separated by a nonmagnetic block layer composed of Ni^{2+} ions located above and below the Mn-vacant sites of the Mn_3O_7 layer, as well as lattice water molecules. The Mn–Mn distance between the layers (6.8 Å) is much greater than the layer thickness (2.8 Å), providing ample room for ion diffusion within the crystal lattice and helping to accommodate the volume changes by reducing the strain that occurs during ion intercalation and extraction process.[23] The spacious layered framework also permits the insertion of water molecules from the electrolyte into the interlayer space.[24] The presence of crystal water in the lattice was confirmed by thermogravimetric analysis measurement (TGA), which showed that V_m-NMO contains 13% lattice water (Fig. 2(c)), consistent with its chemical formula. In comparison, NMO lost 10% of weight

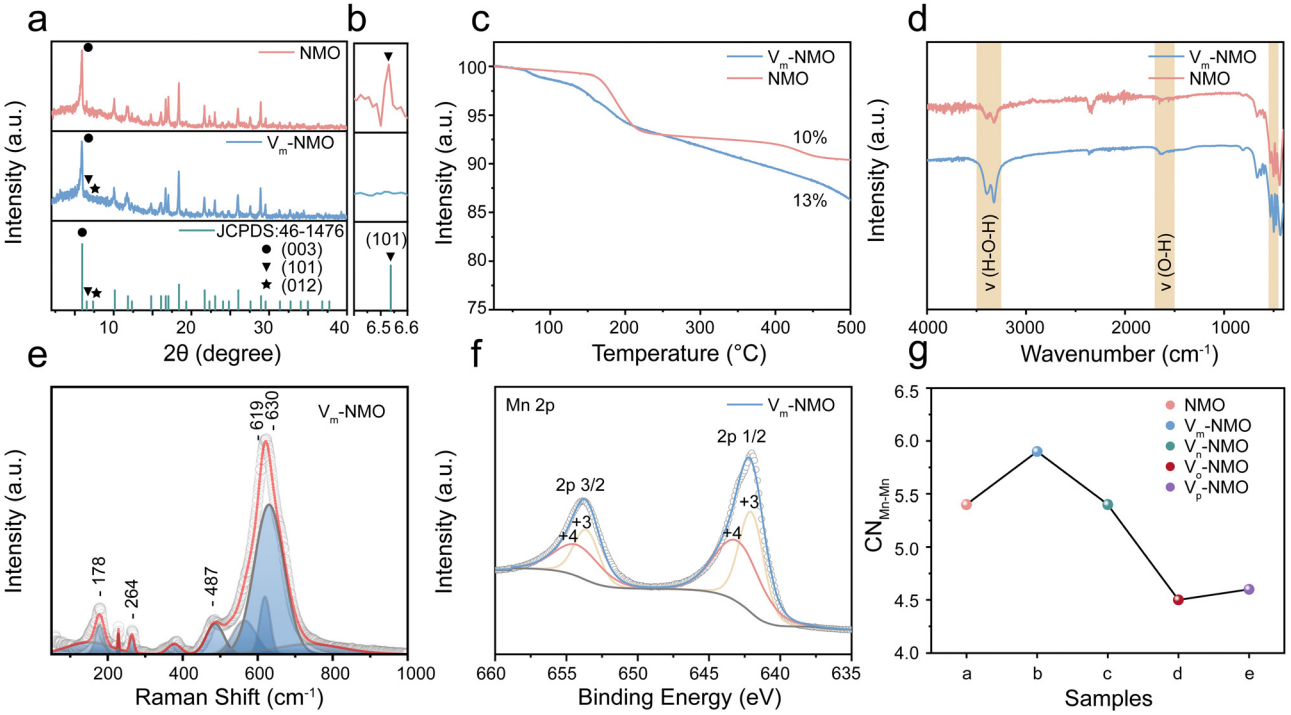

Fig. 2 Material characterisation of as-prepared V_m-NMO and NMO (a) XRD profile. (b) Enlarged XRD profile. (c) TGA profile. (d) FTIR profile. (e) Raman profile. (f) XPS Mn 2p profile. (g) XAFS fitting on the Mn–Mn coordination numbers.

during TGA testing. Previous research confirmed that the lattice water molecules are located at the layered manganese oxide interlayer spaces.[25–28] TGA results indicate that V_m-NMO has a higher crystal water content, which could contribute to building a continuous hydrogen bond network and screening the electrostatic interaction between charge carriers and the host framework.[29] The chemical vibrational modes in the as-prepared materials were confirmed by Fourier transform infrared spectroscopy (FTIR). A series of absorption peaks in Fig. 2(d) could be assigned to different metal oxide vibration modes of Mn–O (530–570 cm^{-1}, 600–620 cm^{-1}), Ni–O (480–490 cm^{-1}) and the vibration of O–H, H–O–H (3200–3400 cm^{-1}) in crystal water, respectively, which are in line with previous research.[30–32] The intensity of the water vibration signals in V_m-NMO is stronger than that in NMO, indicating that V_m-NMO contains more lattice water. The contact angle measurement of the V_m-NMO material is 83°, which is smaller than the contact angle of NMO (122°). The difference in contact angle suggests that the V_m-NMO material has better wettability (ESI,† Fig. S3). Raman spectroscopy was utilised to examine the intricate structural distinctions between V_m-NMO and NMO, employing an excitation wavelength of 532 nm. The V_m-NMO Raman profile showed three distinct bands in the range of 450 to 700 cm^{-1} (Fig. 2(e)): two obvious Raman features at ~490 and ~620–640 cm^{-1} assigned to out-of-plane Mn–O vibrations perpendicular to the layers and the band around 570 cm^{-1} correspond to in-plane Mn–O stretching vibration along with the octahedral layers in V_m-NMO. Raman features of NMO with different vibrational modes were compared to V_m-NMO (ESI,† Fig. S4). A dominant in-plane Mn–O stretching vibration was observed at 571 cm^{-1}, and an out-of-plane Mn–O vibration was found at 621 cm^{-1}. These in-plane and out-of-plane bands are sensitive markers related to the changes in the coordination states of octahedral Mn cations and structural distortions of the related Mn–O environments.[20,33,34] The valence of the as-prepared cathode materials was investigated by X-ray photoelectron spectroscopy (XPS). The Mn 2p XPS profiles shown in Fig. 2(f) and ESI,† Fig. S5 exhibit two distinct peaks in both V_m-NMO and NMO materials, illustrating the co-existence of Mn^{4+} and Mn^{3+}. We found that the ratio of Ni/Mn in V_m-NMO is higher than that of the NMO material. As shown in ESI,† Fig. S6 and S7, the normalised ratios of Ni, Mn, and O in V_m-NMO is about 2 : 13 : 33 while the ratio in NMO is 1 : 13 : 34. This difference can be attributed to the presence of cation vacancies in the V_m-NMO.[35,36] In the crystal structure, cation vacancies create local geometrical distortions and changes in the coordination of neighbouring atoms, leading to an altered distribution of cations within the material. Ni and Mn have similar ionic radii, making Ni a suitable substitute for Mn in the crystal lattice.[37,38] The charge neutrality of the material is maintained by the presence of cation vacancies, which can accommodate the substitution of Ni ions without significantly altering the overall charge balance.[18] The comprehensive analysis of the structural differences between V_m-NMO and NMO was investigated by X-ray absorption fine structure analysis. The Mn–Mn coordination number of V_m-NMO depends on the specific arrangement and concentration of the vacancies, which is an important structural parameter that can influence various material properties, such as electronic structure, transport properties, and reactivity.[39] NMO, V_m-NMO, V_n-NMO, V_o-NMO and V_p-NMO are synthesised by varying the addition of NH_4Cl from 0 mol L^{-1}

to 1 mol L^{-1} while keeping other conditions the same. In Fig. 2(g), an increase in Mn–Mn coordination number was observed in V_m-NMO. This increase can be due to the presence of lattice vacancies, inducing structural rearrangements and facilitating the formation of additional coordination bonds between neighbouring manganese atoms to share their electronic states.[19] With a higher coordination number, there is an expanded overlap of atomic orbitals between adjacent manganese atoms. The overlapping orbitals increase the delocalisation of electronic states and reduce the energy separation between the occupied and unoccupied orbitals. This increased connectivity between manganese atoms lowers the energy barriers that charges need to overcome to move between adjacent sites. Charge carriers, including proton and zinc ions, can more easily transfer from one manganese atom to another, enabling more efficient charge storage.[40–42]

Multiple techniques were employed to thoroughly examine the morphology and understand the role of vacancies in as-prepared materials. Scanning electron microscope (SEM) was used to analyse the morphology of V_m-NMO, revealing a homogeneous three-dimensional flower-like particle composed of nanoplates, as shown in ESI,† Fig. S8. The structural symmetry and crystallinity of as-prepared V_m-NMO materials were studied using transmission electron microscopy (Fig. 3(a)), which showed that an average length of V_m-NMO nanoplate is 150 nm. An inter-layer distance of 0.68 nm in the V_m-NMO was illustrated by high-resolution transmission electron microscopy (HRTEM) (ESI,† Fig. S9), which corresponds to the (003) lattice plane in V_m-NMO. This lattice space result is consistent with relevant XRD findings. The elemental mapping results demonstrated that Ni, Mn, and O are uniformly distributed across V_m-NMO nanoplates and NMO nanorods (ESI,† Fig. S10–S14). Scanning transmission electron microscopy (STEM) images provide atomic-level insights into lattice distortion and defects within V_m-NMO lattice (Fig. 3(b)). Atomic-resolution STEM images of V_m-NMO show direct evidence of atomically scattered Mn vacancies throughout the V_m-NMO nanoplate (Fig. 3(c)). Lattice vacancies can facilitate hydrated proton transfer by lowering the energy barrier, which enables Grotthuss topochemistry. The k^3-weighted Fourier transform of the extended X-ray absorption fine structure (EXAFS) can provide information about the local atomic environment surrounding Mn atoms.[43] The Mn K-edge EXAFS spectrum of the as-prepared materials showed two peaks located at 1.5 Å and 2.5 Å, corresponding to the Mn–O (the six coordinated oxygen atoms of the nearest neighbouring atom around the manganese atom) and Mn–Mn (six coordinated manganese atom edge sharing through oxygen atom within $[MnO_6]$ octahedral slab) shells, respectively. The position and intensity of these peaks provide information about the Mn–O and Mn–Mn bond length and coordination number in the material. A reduction in Mn–Mn peak intensity was observed in the V_m-NMO sample, suggesting a reduction in the coordination number of Mn cations in the V_m-NMO material. It is demonstrated that the local structure of the V_m-NMO material possesses defects in the crystal lattice. This reduction further supports the presence of Mn vacancies in V_m-NMO[44,45]

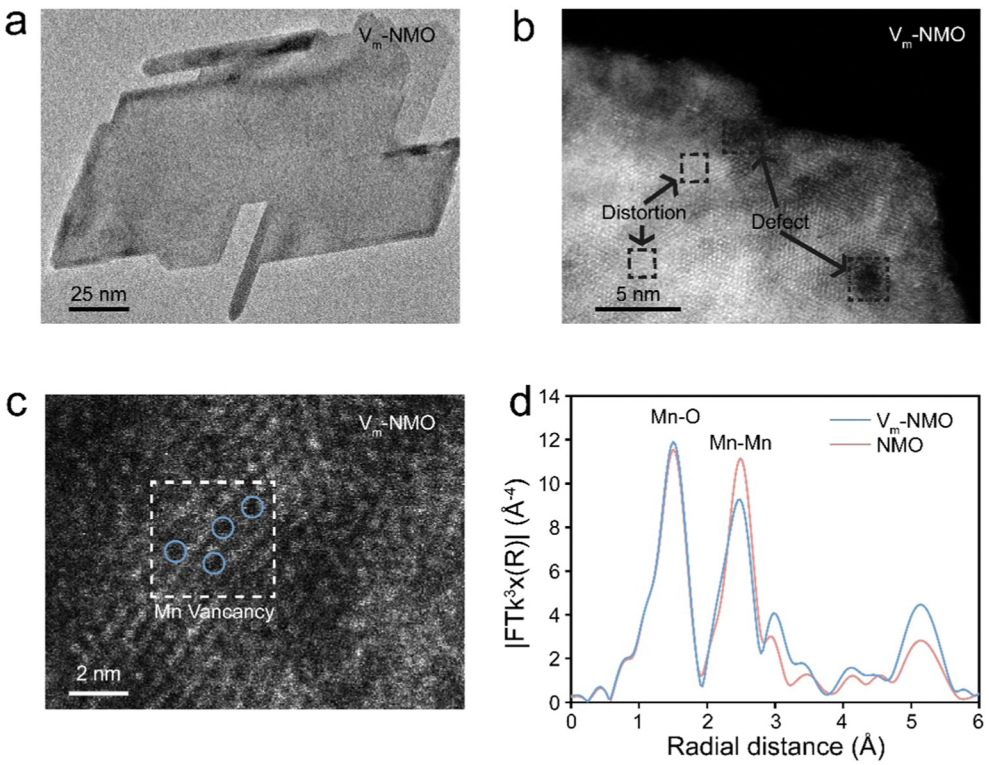

Fig. 3 Material characterisation of as-prepared $NiMn_3O_7{\cdot}3H_2O$ (a) TEM profile. (b) HRTEM profile. (c) Atomic resolution STEM profile. (d) k^3-weighted Fourier transform of the extended X-ray absorption fine structure data for V_m-NMO and NMO.

Computational simulation on proton migration

To further gain insight into the proton hopping mechanism with and without cationic (Mn^{4+}) vacancies in the $NiMn_3O_7$ (001) system, density functional theory (DFT) based quantum chemical calculations were performed using the Vienna Ab initio Simulation Package (VASP).[41,46] We note that while our experimental results indicated the dominance of the (003) facet of $NiMn_3O_7$, we chose to focus on the (001) facet for the sake of simplicity in our calculations, allowing meaningful comparisons and benchmarking with previous theoretical studies.[17,47–49] At first, the stable sites for proton adsorption on the $NiMn_3O_7$ (001) surface were evaluated (Fig. 4(a)). For these calculations, three models were considered, *i.e.*, (i) proton in the proximity of the crystal water molecules between the $NiMn_3O_7$ layers, (ii) proton bonded to an Mn^{4+} ion and (iii) proton bonded to an O^{2-} ion on the $NiMn_3O_7$ layers. The fully relaxed geometries revealed that in (i) and (ii) above, the protons were transferred to a nearby O^{2-} ion and, in the third case, remained adsorbed on the O^{2-} ion (ESI,† Fig. S15). The adsorption of protons is favoured on the O^{2-} ions of the $NiMn_3O_7$ layers. Previously, it was reported that the transition metal vacancies (Mn, Cd, Zn) could contribute to easy proton absorption/desorption and enable exceptionally high proton conduction.[50–55] Our experiments also evidenced the presence of Mn^{4+} vacancies in the $NiMn_3O_7$ system.

Therefore, in the next step, the adsorption of a proton was carried out around an Mn^{4+} defect, *i.e.*, (iv) on an O^{2-} ion next to the defect site, (v) on another O^{2-} ion away from the defect site and (vi) on the defect site. The relaxed structures showed that in the fourth and fifth cases, the proton remained bonded to the O^{2-} ions, but in the sixth case, as expected, the proton migrated to a nearby O^{2-} ion close to the defect site (ESI,† Fig. S16). The calculated adsorption energies of the protons in the pristine models without Mn^{4+} vacancies are in the range of −2.97 eV to −3.07 eV, while in the models with Mn^{4+} vacancies, they are in the range of −4.03 eV to −5.07 eV (ESI,† Fig. S17). This indicates higher stability of protons in the V_m-NMO systems with cationic vacancies. The Bader charges of −1.13 eV and −1.21 eV on the O^{2-}, respectively for $NiMn_3O_7$ systems without and with Mn^{4+} respectively indicate that this may be due to relatively larger charge localisation in the defective model. Additionally, within the $NiMn_3O_7$ system with Mn^{4+} defect, we found that when protons are adsorbed on the O^{2-} ions close to the defect site, they are ∼−1.04 eV more stable than when they are slightly further away. This difference indicates that the protons could easily hop to a site closer to the defect site. As shown in Fig. 4(d), the calculated energy barriers for proton hopping between two consecutive O^{2-} ions in the absence (*i.e.*, 0.79 eV) and presence (*i.e.*, 0.56 eV) further support these findings. Therefore, from the DFT calculations, we conclude that Mn^{4+} vacancies are the driving force for proton hopping in $NiMn_3O_7$.

Electrochemical performance of V_m-NMO and NMO materials

To systematically study the electrochemical performance of the defective material for AZIBs, we prepared cathode materials

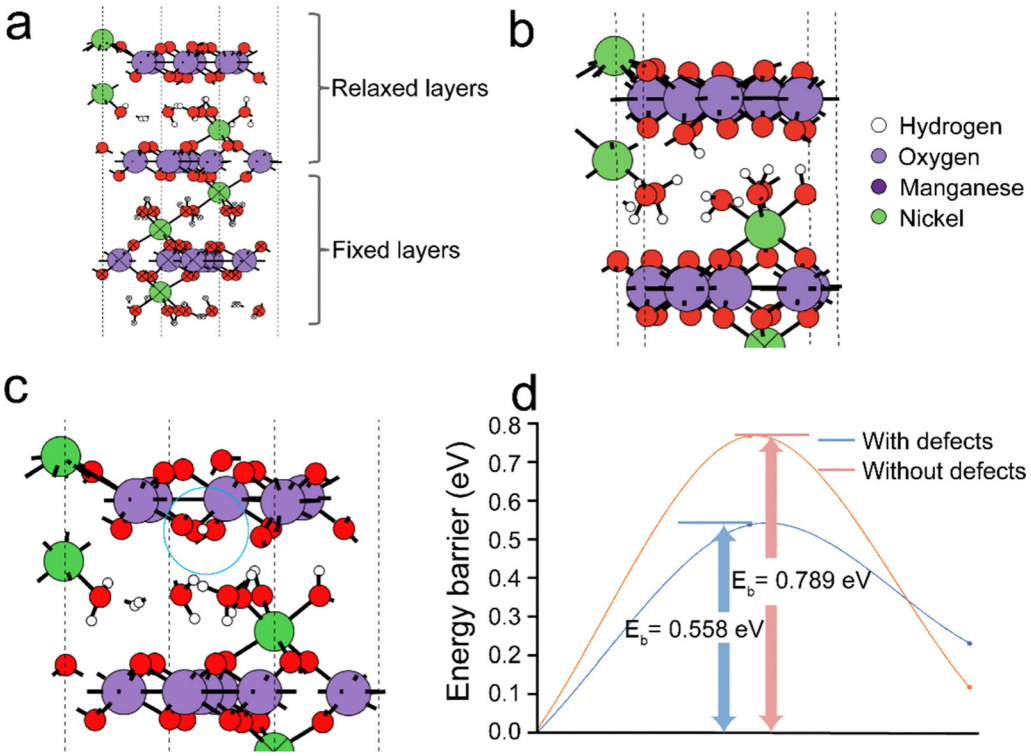

Fig. 4 (a) Fully relaxed pristine $NiMn_3O_7$ (001) model showing the positions of different ions and interlayer water molecules. To properly reproduce the majority of the structure, the position of the bottom two layers of $NiMn_3O_7$ and water crystal molecules are held constant. Fully relaxed geometries of adsorbed protons in the $NiMn_3O_7$ (001) surface (b) without and (c) with Mn^{4+} defects and (d) the energy barriers of proton hopping with and without Mn^{4+} defects.

and investigated them using cyclic voltammetry (CV) curves in Swagelok cells with zinc metals as the anode. The CV curves of NMO reveal two pairs of redox peaks, corresponding to proton intercalation/deintercalation at ~1.12 V/1.63 V and zinc ion intercalation/deintercalation at ~1.35 V/1.57 V. In contrast, V_m-NMO cathode material exhibits reduced polarisation of redox reactions (187 mV *vs.* 210 mV), implying enhanced ion transport.[56] The presence of Mn^{4+} vacancies in V_m-NMO and its lattice water network can create pathways for Grotthuss conduction, enabling the electrode to be charged and discharged close to theoretical capacity and maintain stability for thousands of cycles. Moreover, as shown in ESI,† Fig. S18, the CV curves of V_m-NMO remain unchanged after first cycle activation, demonstrating the high reversibility. The galvanostatic intermittent titration technique (GITT) was employed to estimate the diffusion coefficient of Zn^{2+} ($D_{Zn^{2+}}$) in V_m-NMO material with manganese vacancies. Fig. S19 (ESI†) illustrates that the average $D_{Zn^{2+}}$ values at the charge and discharge plateaus are approximately 10^{-10} to 10^{-11} cm^2 s^{-1}, respectively. This Zn diffusivity is comparable to the Li diffusion coefficient (typically 10^{-10} cm s^{-1}) reported in the literature. In contrast, the NMO electrode exhibits a lower $D_{Zn^{2+}}$ (10^{-11} to 10^{-12} cm^2 s^{-1}) and a larger overpotential, indicating the sluggish charge/discharge mobility. The electrochemical impedance spectroscopy (EIS) reveals that V_m-NMO defective cathode material with a hydrogen-bonding network promotes charge transfer. The charge transfer resistance of V_m-NMO (43 Ω) is significantly lower than NMO (75 Ω), illustrating that manganese vacancies with a continuous hydrogen bond network within the V_m-NMO lattice could enhance charge transfer in the system. The galvanostatic charge–discharge curves of V_m-NMO and NMO cathode materials are illustrated in Fig. 5(c), and these were obtained under various current densities, ranging from 0.2 to 5 A g^{-1}, with eight cycles at each current density. Noticeable charge and discharge plateaus could be observed, with a high specific capacity of 318 mA h g^{-1} achieved at 0.2 A g^{-1}. The V_m-NMO cathode material possesses substantial cycling performance (91% over one hundred cycles). Moreover, the specific capacity retains 38% after increasing the current density 25-fold to 5 A g^{-1}. The detailed cycling and rate performance are illustrated in Fig. 5(d). As the current density increases stepwise, the corresponding specific capacity is retained at 254, 215, 173 and 121 mA h g^{-1} at 0.5, 1, 2 and 5 A g^{-1}, respectively. After the current density returns to 0.2 A g^{-1}, the specific capacity recovers, demonstrating stable charge/discharge performances under different current densities. The remarkable rate performance enables V_m-NMO to maintain stably under high current densities, with a capacity retention of 91% over 4000 cycles (Fig. 5(f)). In contrast, the rate performance of NMO under identical conditions is lower than that of V_m-NMO, indicating superior ion transport in the V_m-NMO cathode material.

Kinetic evaluation on the V_m-NMO and NMO cathode materials

To further investigate the influence of the Grotthuss mechanism on the intercalation process in AZIBs, we analysed the electrochemical processes of V_m-NMO and NMO using CV tests at multiple scan rates. The *b* value, capacitive contributions, and capacitive ratios of V_m-NMO and NMO were compared in Fig. 6. As shown in Fig. 6(a), two pairs of redox peaks (C1/D1 and C2/D2) appeared in the CV curve of V_m-NMO, and these redox peak positions shifted with increasing scan rate. To investigate the diffusion behaviour in V_m-NMO, the corresponding processes of

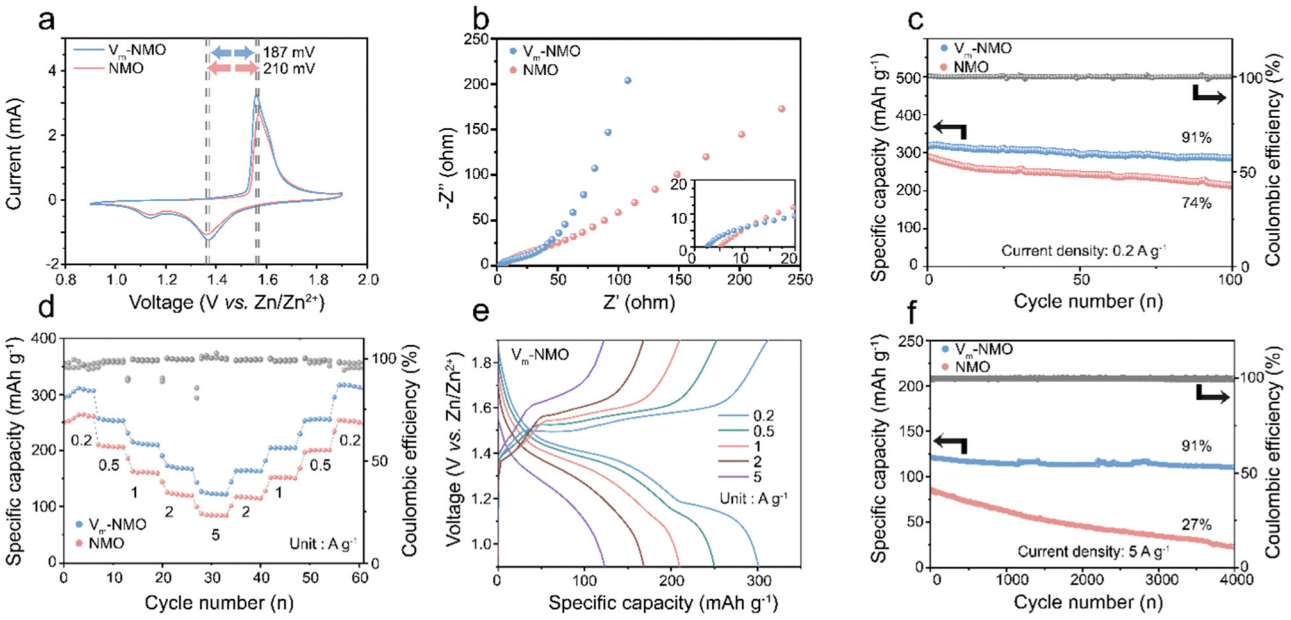

Fig. 5 Electrochemical performances of as-prepared Zn||V_m-NMO batteries. (a) CV curves of as-prepared materials at different scan rates. (b) EIS profiles of V_m-NMO and NMO. (c) Cycling performance of V_m-NMO and NMO at the current density of 0.2 A g^{-1}. (d) Rate performance. (e) Galvanostatic charge–discharge profiles of V_m-NMO cathodes at different current densities; (f) cycling performance of Zn||V_m-NMO and Zn||NMO batteries at the current density of 5 A g^{-1}.

charge storage were calculated according to the linear relationship between log *i versus* log *v* using the equation below:

$$i = av^b \quad (1)$$

In this equation, the peak current *i* and sweep rate *v* were directly obtained, and *a*, *b* are parameters that change accordingly. The value of *b* within a range of 0.5 to 1 implies different charge storage behaviour with respect to capacitive (*b* = 1) and diffusion-controlled (*b* = 0.5) behaviours. Accordingly, the linear fitting *b* values result from the CV curves of both V_m-NMO and NMO were between 0.5 to 1, indicating that the ion storage behaviour comprises both diffusion-controlled and capacitive behaviours. In Fig. 6(b), the *b* values of V_m-NMO are 0.60, 0.92, 0.62, and 0.97, indicating an enhanced capacitive behaviour that could contribute to faster ion storage kinetics. In comparison, the *b* values of NMO (Fig. 6(d)) are obviously lower than that of V_m-NMO, indicating a sluggish ion storage process. These results indicate that an improved ion transfer ability is due to the fast displacive hydrated proton hopping mechanism. To further illustrate the storage behaviour of V_m-NMO, capacitive contribution ratios were revealed under different scan rates (Fig. 6(e)–(h)). The capacitive behaviour contributes to 41% of overall storage at a scan rate of 0.1 mV s^{-1}, and this ratio gradually increases to 46% as the scan rate rises to 0.5 mV s^{-1}. In contrast, NMO exhibits only 18% of capacitive behaviour under a scan rate of 0.1 mV s^{-1}. A similar trend is observed at different scan rates, indicating that capacitive behaviour is enhanced (ESI,† Fig. S20 and S21), which aligns with the *b* value results. These results indicate the enhancement in charge transfer can be attributed to the facilitated displacive hydrated proton hopping, which creates pathways for efficient ion migration.

Electrochemical insertion/deinsertion reaction mechanism

Ex situ XPS tests were conducted to uncover the valence changes during the charging and discharging.[57] Fig. 7(a) illustrates the classic manganese valence change in AZIBs. The Mn 2p spectra fitting results, featuring two deconvoluted peaks, indicate a mixture of multiple Mn valence states.[58] In the discharging state, the manganese valence peak position undergoes a negative shift, signifying the reduction of manganese oxide compared to the pristine state due to charge carrier intercalation. During the charging process, Mn 2p peaks shift positively toward the pristine position, indicating reversible valence changes throughout charge and discharge cycles.[59–63] Fig. 7(b) and Fig. S22 (ESI†) demonstrate a persistent Ni 2p signal in various states, confirming the stability of nickel atoms in the cathode material, where it balances the charge induced by vacancies. The nickel atoms in V_m-NMO remain inactive during charging and discharging cycles, with interlayer nickel ions compensating for the charge imbalance caused by manganese vacancy and contributing to cycling stability. In contrast, the Ni 2p XPS intensity of cycled NMO electrode decreased, indicating a partial deintercalation of nickel in NMO electrodes upon cycling. Fig. 7(d) and (e) show *ex situ* XRD results that reveal characteristic peaks associated with the discharging process of the V_m-NMO electrode. The reversible peak appearance and disappearance of the zinc hydroxide trifluoromethyl sulfonate peak at the low degree indicates the proton intercalation during the discharging process.[64,65] Consistent with numerous manganese-based materials studies, zinc hydroxide trifluoromethyl sulfonate forms through the integration of OH^-, $Zn(CF_3SO_3)_2$, and H_2O in the electrolyte following proton transfer to the V_m-NMO electrode.[66,67] The characteristic peaks disappear in the subsequent charging phase, implying a reversible reaction. The formation and disappearance of XRD characteristic peaks highlight the reversible proton transfer during the discharging process.

Mn L-edge Near Edge X-ray Absorption Fine Structure (NEXAFS) spectra provide insights into the local bonding environment of manganese atoms in the cathode material. The pristine

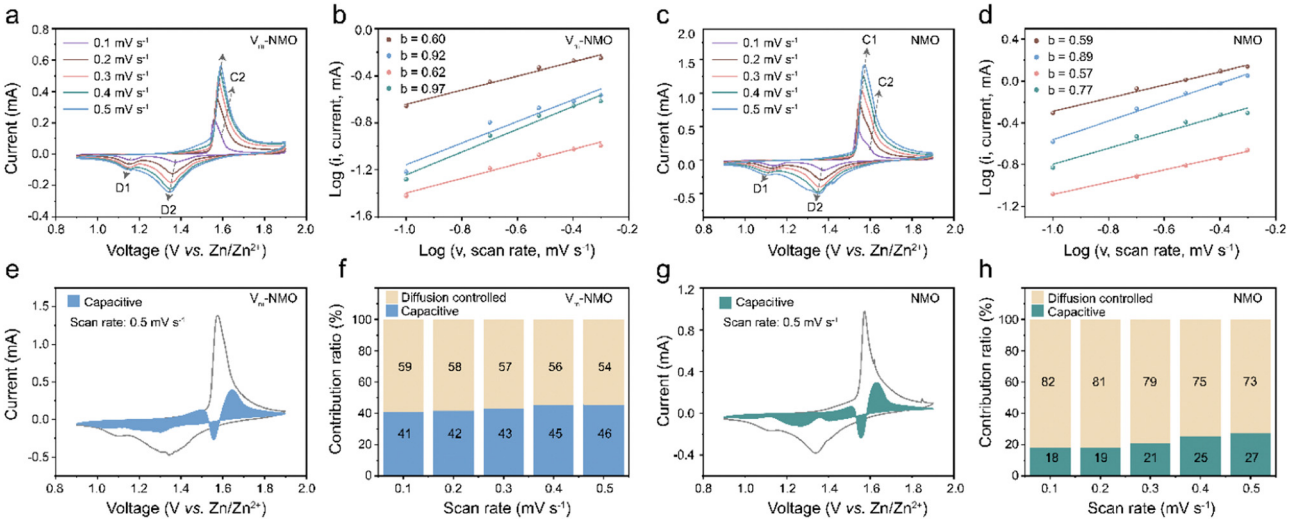

Fig. 6 Electrochemical characterisation of as-prepared $NiMn_3O_7{\cdot}3H_2O$. (a) CV plots of V_m-NMO at different scan rates. (b) *b*-value of V_m-NMO. (c) CV plots of NMO in different scan rates. (d) *b*-value of NMO. (e) Capacitive contribution of V_m-NMO at the scan rate of 0.5 mV s^{-1}. (f) Capacitive ratio of V_m-NMO in different scan rates. (g) Capacitive contribution of NMO at the scan rate of 0.5 mV s^{-1}. (h) Capacitive ratio of NMO under different scan rates.

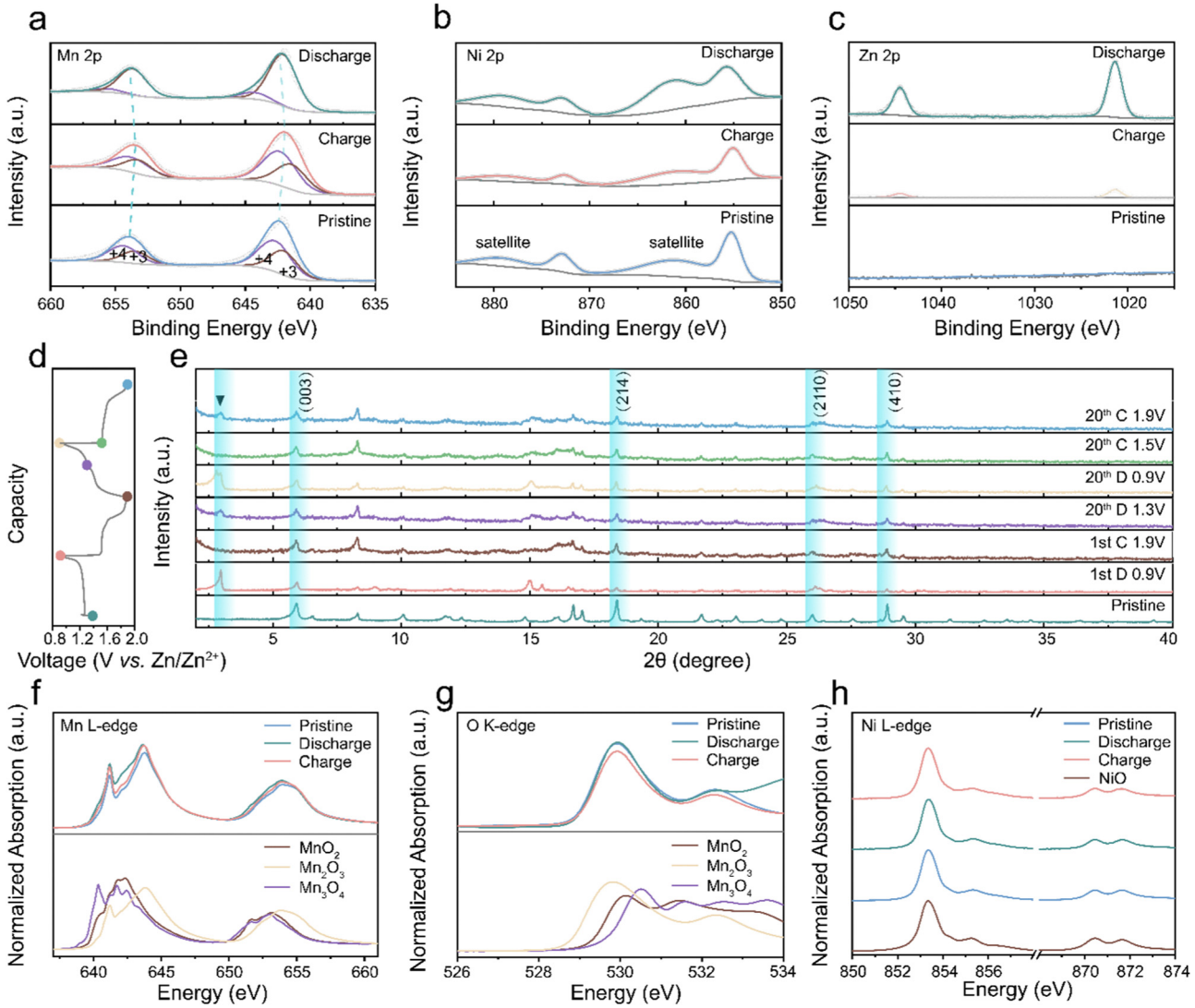

Fig. 7 The charge storage mechanism of V_m-NMO batteries. *Ex situ* XPS profiles of V_m-NMO at different states: (a) Mn 2p. (b) Ni 2p. (c) Zn 2p. (d) and (e) *Ex situ* XRD profiles of V_m-NMO at different states. (f) Mn $L_{3,2}$-edge NEXAFS profiles at different states. (g) O K-edge NEXAFS profiles of cathode materials in different states. (h) NEXAFS profiles of Ni L-edge of cathode materials in different states.

state spectrum exhibits multiple peaks corresponding to different electronic transitions and variations in coordination environment with oxygen atoms, namely A (638–639 eV, 2p–3d, octahedral), B (641–642 eV, 2p–3d, tetrahedral), C (643–644 eV, 2p–3d, mixed octahedral and tetrahedral sites).[68] This indicates that the Mn ions in V_m-NMO can occupy both octahedral and tetrahedral sites, particularly Mn ions situated at the edge or corner sites of MnO_6 octahedral units. The crystal structure of V_m-NMO comprises edge-sharing MnO_6 octahedra layers interconnected by sharing corners with other octahedra. Fig. 7(f) of Mn $L_{3,2}$-edge NEXAFS reveals that the shape of V_m-NMO in the charging and pristine state resembles MnO_2(IV), verifying that pristine valence is close to +4 and Mn valence can be reduced to pristine in the charging state. The systematic shift of the L_3 leading edge position and gravity centre of the L_3/L_2 edge towards lower energies is observable in the fully discharging state, indicating that the Mn oxidation state in the discharging state is lower than in the pristine state and the fully charging state. Additionally, the Mn L-edge intensity between 641–642 eV increased in the discharging state, the similarity in the peak shape to Mn^{3+}, indicating Mn atoms were reduced to a valence close to Mn(III) in the discharged state after zinc ion intercalation. Moreover, O K-edge NEXAFS spectra, determined by the hybridisation of O 2p and Mn 3d states, lead to electron transitions from ligand O 1s orbitals to unoccupied transition metal 3d orbitals. In Fig. 7(g), the O K-edge spectra include several distinct peaks around 529 eV and 532 eV. In the pristine and fully charging state, two absorption peaks can be identified due to the Mn(IV) with a $3d^3$ ($t_{2g}^3e_g^0$) configuration, while a lower energy peak belongs to spin-down t_{2g} and spin-up e_g transitions, and a higher energy peak originate from the spin-down e_g transitions. In the fully discharged state, the peak intensity increases with a broad absorption peak identifiable between 530–531 eV, caused by the Mn(III) content with a $3d^4$ ($t_{2g}^3e_g^1$)

configuration. The octahedral layers in $NiMn_3O_7$ are separated by tetrahedral voids occupied by nickel cations.[23,69] In the charging state, Ni L-edge NEXAFS spectroscopy provides valuable information about the oxidation state of Ni and the coordination environment of Ni atoms in the material. The NEXAFS spectrum offers insight into the redox activity and stability of nickel ions in the material. The peak A (853 eV) and peak B (855 eV) are attributed to transitions from Ni $2p_{3/2}$ core level to the unoccupied 3d orbitals and unoccupied 4p orbitals, respectively. The intensity of these two peaks depends on the oxidation state of the Ni ions and is sensitive to changes in the local coordination environment of the Ni atoms. The multiple peaks in Fig. 7(h) illustrate the high spin Ni^{2+} electronic structure and its octahedral coordination structure. The intensity and peak position remain stable in the charging and discharging states, indicating that Ni^{2+} is electrochemically stable in the V_m-NMO lattice. Nickel ions facilitate the ongoing mobility of hydrated protons *via* Grotthuss hopping by preserving the system's electrical neutrality, which counterbalances the dynamic changes caused by proton migration.

Conclusion

In summary, our research demonstrates the synergistic collaboration between vacancies, lattice water and nickel ions on enhancing the hydrated protons hopping *via* the Grotthuss mechanism for high-performance zinc ion battery cathodes. Energy barrier calculations for proton transfer with and without Mn^{4+} vacancies indicate that proton transfer is favoured in the presence of defects. Mn^{4+} vacancies act as the driving force for proton hopping in the V_m-NMO systems. Additionally, the presence of lattice water molecules within the host material facilitates the migration of hydrated protons from the electrolyte to the interlayer spaces in the lattice. The simulation results indicate that protons prefer to bond with O^{2-} ions on the Mn–O layer rather than staying with water molecules. The continuous hopping of protons within the host material induces periodic, temporary local structural changes in the lattice. This dynamic behaviour alters the energy barriers for ion intercalation and deintercalation, thereby optimising their diffusion pathways. Moreover, the presence of manganese vacancies in the lattice serve as additional sites for hydrated proton and zinc ion intercalation, resulting in an increased capacity. The nickel ions increase the stability by preserving the system's electrical neutrality. The as-prepared V_m-NMO cathode material exhibits enhanced ion transfer and a high specific capacity of 318 mA h g^{-1} at 200 mA g^{-1}. Furthermore, it demonstrates excellent rate performances, and remarkable cycling stability, with a capacity retention of 91% over 4000 cycles. Overall, this study provides insights into the utilisation of the Grotthuss mechanism and manganese oxide's distinct characteristics for the advancement of energy storage technologies. These findings highlight the potential of utilising the Grotthuss mechanism to develop high-performance energy storage materials.

Author contributions

F. Z.: conceptualisation, methodology, software, data acquisition, data curation, formal analysis, investigation, validation, visualisation, writing – original draft, and writing – review and editing. J. L.: conceptualisation, methodology, formal analysis, and writing – review and editing. A. C.: conceptualisation, data acquisition, formal analysis, software, and writing – review and editing. L. L., L. K., H. D., X. G., and Y. T.: data acquisition, software, formal analysis. F. L., T. L.: methodology, data acquisition, and writing – review and editing. I. P.: funding acquisition, supervision, and writing – review and editing. G. H.: conceptualisation, methodology, funding acquisition, supervision, and writing – review and editing.

Conflicts of interest

There are no conflicts to declare.

Acknowledgements

The authors would like to thank the Engineering and Physical Sciences Research Council (EPSRC, EP/V027433/3), EPSRC Centre for Doctoral Training in Molecular Modelling and Materials Science (EP/L015862/1), UK Research and Innovation (UKRI) under the UK government's Horizon Europe funding (101077226; EP/Y008707/1), Open Foundation of the State Key Laboratory of Silicate Materials for Architectures at WUT (no. SYSJJ2020-04), Shanghai Scientific and Technological Innovation Project (22520710100) and the Royal Society (RGS/R1/211080; IEC/NSFC/201261) for funding support. AC acknowledges the use of the Sulis Tier 2 HPC platform at the University of Warwick funded by EPSRC (EP/T022108/1) and ARCHER2 *via* the membership of the UK's HEC Materials Chemistry Consortium funded by EPSRC (EP/R029431). We acknowledge the B18 beamline (proposal no. SP32905), B07-B beamline (proposal no. SI29340), and electron Physical Science Imaging Centre instruments E01 and E02 (proposal no. MG32058, MG32035) at Diamond Light Source for the allocated experiment sessions. We thank Dr Iuliia Mikulska, Dr Veronica Celorrio, and Dr Diego Gianolio for their support during our B18 beamtime session, and Dr Pilar Ferrer and Dr David C. Grinter for their support during our B07-B beamtime session, and Dr David G. Hopkinsonc and Dr Christopher S. Allen for their support during our STEM session. We thank Prof. K. Holt for the discussion on FTIR spectrum.

References

1 J. B. Goodenough and Y. Kim, *Chem. Mater.*, 2009, **22**, 587–603.
2 B. Tang, L. Shan, S. Liang and J. Zhou, *Energy Environ. Sci.*, 2019, **12**, 3288–3334.
3 R. H. Tunuguntla, F. I. Allen, K. Kim, A. Belliveau and A. Noy, *Nat. Nanotechnol.*, 2016, **11**, 639–644.

4 I. Popov, Z. Zhu, A. R. Young-Gonzales, R. L. Sacci, E. Mamontov, C. Gainaru, S. J. Paddison and A. P. Sokolov, *Commun. Chem.*, 2023, **6**, 77.
5 C. Dellago, M. M. Naor and G. Hummer, *Phys. Rev. Lett.*, 2003, **90**, 105902.
6 Z. Cao, Y. Peng, T. Yan, S. Li, A. Li and G. A. Voth, *J. Am. Chem. Soc.*, 2010, **132**, 11395–11397.
7 C. Dellago and G. Hummer, *Phys. Rev. Lett.*, 2006, **97**, 245901.
8 X. Wu, J. J. Hong, W. Shin, L. Ma, T. Liu, X. Bi, Y. Yuan, Y. Qi, T. W. Surta, W. Huang, J. Neuefeind, T. Wu, P. A. Greaney, J. Lu and X. Ji, *Nat. Energy*, 2019, **4**, 123–130.
9 T. Miyake and M. Rolandi, *J. Phys.: Condens. Matter*, 2016, **28**, 023001.
10 H. Zhang, W. Wu, Q. Liu, F. Yang, X. Shi, X. Liu, M. Yu and X. Lu, *Angew. Chem., Int. Ed.*, 2021, **60**, 896–903.
11 W. Sun, Z. Xu, C. Qiao, B. Lv, L. Gai, X. Ji, H. Jiang and L. Liu, *Adv. Sci.*, 2022, **9**, e2201679.
12 N. Zhang, F. Cheng, Y. Liu, Q. Zhao, K. Lei, C. Chen, X. Liu and J. Chen, *J. Am. Chem. Soc.*, 2016, **138**, 12894–12901.
13 T. Xiong, Z. G. Yu, H. Wu, Y. Du, Q. Xie, J. Chen, Y. W. Zhang, S. J. Pennycook, W. S. V. Lee and J. Xue, *Adv. Energy Mater.*, 2019, **9**, 1803815.
14 G. Fang, C. Zhu, M. Chen, J. Zhou, B. Tang, X. Cao, X. Zheng, A. Pan and S. Liang, *Adv. Funct. Mater.*, 2019, **29**, 1808375.
15 Y. Fu, Q. Wei, G. Zhang, X. Wang, J. Zhang, Y. Hu, D. Wang, L. Zuin, T. Zhou, Y. Wu and S. Sun, *Adv. Energy Mater.*, 2018, **8**, 1801445.
16 J. Li, N. Luo, L. Kang, F. Zhao, Y. Jiao, T. J. Macdonald, M. Wang, I. P. Parkin, P. R. Shearing, D. J. L. Brett, G. Chai and G. He, *Adv. Energy Mater.*, 2022, **12**, 2201840.
17 D. Chao, W. Zhou, C. Ye, Q. Zhang, Y. Chen, L. Gu, K. Davey and S. Z. Qiao, *Angew. Chem., Int. Ed.*, 2019, **58**, 7823–7828.
18 Z. Ma, X. M. Shi, S. I. Nishimura, S. Ko, M. Okubo and A. Yamadas, *Adv. Mater.*, 2022, **34**, e2203335.
19 S.-i Ohkoshi, K. Nakagawa, K. Tomono, K. Imoto, Y. Tsunobuchi and H. Tokoro, *J. Am. Chem. Soc.*, 2010, **132**, 6620–6621.
20 D. Chen, D. Ding, X. Li, G. H. Waller, X. Xiong, M. A. El-Sayed and M. Liu, *Chem. Mater.*, 2015, **27**, 6608–6619.
21 Y. Zhang, H. Zhang, L. Fang, J. Deng and Y. Wang, *Electrochim. Acta*, 2017, **245**, 32–40.
22 F. Putzolu, G. Balassone, M. Boni, M. Maczurad, N. Mondillo, J. Najorka and F. Pirajno, *Ore Geol. Rev.*, 2018, **97**, 21–34.
23 Y. Haraguchi, A. Matsuo, K. Kindo and Z. Hiroi, *Phys. Rev. B*, 2018, **98**, 064412.
24 D. Kundu, B. D. Adams, V. Duffort, S. H. Vajargah and L. F. Nazar, *Nat. Energy*, 2016, **1**, 16119.
25 X. Jia, C. Liu, Z. G. Neale, J. Yang and G. Cao, *Chem. Rev.*, 2020, **120**, 7795–7866.
26 K. W. Nam, H. Kim, J. H. Choi and J. W. Choi, *Energy Environ. Sci.*, 2019, **12**, 1999–2009.
27 D. Yuan, X. Li, H. Yao, Y. Li, X. Zhu, J. Zhao, H. Zhang, Y. Zhang, E. T. J. Jie, Y. Cai and M. Srinivasan, *Adv. Sci.*, 2023, **10**, 2206469.
28 C. Xia, J. Guo, Y. Lei, H. Liang, C. Zhao and H. N. Alshareef, *Adv. Mater.*, 2018, **30**, 1705580.
29 K. W. Nam, H. Kim, J. H. Choi and J. W. Choi, *Energy Environ. Sci.*, 2019, **12**, 1999–2009.
30 L. Kang, M. Zhang, Z.-H. Liu and K. Ooi, *Spectrochim. Acta*, 2007, **67**, 864–869.
31 X. Xie, J. Li, Z. Xing, B. Lu, S. Liang and J. Zhou, *Nat. Sci. Rev.*, 2023, **10**, nwac281.
32 R. Yi, X. Shi, Y. Tang, Y. Yang, P. Zhou, B. Lu and J. Zhou, *Small Struct.*, 2023, **4**, 2300020.
33 Z. M. Chan, D. A. Kitchaev, J. N. Weker, C. Schnedermann, K. Lim, G. Ceder, W. Tumas, M. F. Toney and D. G. Nocera, *Proc. Natl. Acad. Sci. U. S. A.*, 2018, **115**, E5261–E5268.
34 Y.-K. Hsu, Y.-C. Chen, Y.-G. Lin, L.-C. Chen and K.-H. Chen, *Chem. Commun.*, 2011, **47**, 1252–1254.
35 Y. Li, Y. Lu, X. Jiang, L. Lu, J. Qin, D. Yang, J.-L. Chen, L. Zhang, D. Wang and A. Lei, *Energy Storage Mater.*, 2023, **54**, 553–562.
36 H. Qin, Y. Ye, J. Li, W. Jia, S. Zheng, X. Cao, G. Lin and L. Jiao, *Adv. Funct. Mater.*, 2023, **33**, 2209698.
37 S. Mazen, N. Abu-Elsaad and A. Nawara, *Phys. Solid State*, 2020, **62**, 1183–1194.
38 C. Liang, F. Kong, R. C. Longo, C. Zhang, Y. Nie, Y. Zheng and K. Cho, *J. Mater. Chem.*, 2017, **5**, 25303–25313.
39 J. Schmalhorst, A. Thomas, S. Kämmerer, O. Schebaum, D. Ebke, M. Sacher, G. Reiss, A. Hütten, A. Turchanin and A. Gölzhäuser, *Phys. Rev. B: Condens. Matter Mater. Phys.*, 2007, **75**, 014403.
40 J. H. Lee, G. Ali, D. H. Kim and K. Y. Chung, *Adv. Energy Mater.*, 2017, **7**, 1601491.
41 G. Kresse and J. Hafner, *Phys. Rev. B: Condens. Matter Mater. Phys.*, 1994, **49**, 14251–14269.
42 J. Li, Z. Liu, S. Han, P. Zhou, B. Lu, J. Zhou, Z. Zeng, Z. Chen and J. Zhou, *Nano-Micro Lett.*, 2023, **15**, 237.
43 P. Bhobe, K. Priolkar and P. Sarode, *Phys. Rev. B*, 2006, **74**, 224425.
44 T. Ressler, S. L. Brock, J. Wong and S. L. Suib, *J. Phys. Chem. B*, 1999, **103**, 6407–6420.
45 F. Wang, J. Deng, S. Impeng, Y. Shen, T. Yan, G. Chen, L. Shi and D. Zhang, *Chem. Eng. J.*, 2020, **396**, 125192.
46 G. Kresse and J. Furthmüller, *Phys. Rev. B: Condens. Matter Mater. Phys.*, 1996, **54**, 11169–11186.
47 W. Yang, Y. Zhu, F. You, L. Yan, Y. Ma, C. Lu, P. Gao, Q. Hao and W. Li, *Appl. Catal., B*, 2018, **233**, 184–193.
48 C. Y. Ouyang, Ž. Šljivančanin and A. Baldereschi, *J. Chem. Phys.*, 2010, **133**, 204701.
49 J. A. Dawson, H. Chen and I. Tanaka, *ACS Appl. Mater. Interfaces*, 2015, **7**, 1726–1734.
50 H. Lind, B. Wickman, J. Halim, G. Montserrat-Sisó, A. Hellman and J. Rosen, *Adv. Sustain. Syst.*, 2021, **5**, 2000158.
51 L. Li, X. Feng, Y. Nie, S. Chen, F. Shi, K. Xiong, W. Ding, X. Qi, J. Hu, Z. Wei, L.-J. Wan and M. Xia, *ACS Catal.*, 2015, **5**, 4825–4832.
52 B. Ammundsen, D. J. Jones, J. Roziere and G. R. Burns, *Chem. Mater.*, 1995, **7**, 2151–2160.

53 W. Zhao, X. Feng, W. Tan, F. Liu and S. Ding, *J. Environ. Sci.*, 2009, **21**, 520–526.
54 E. Silvester, A. Manceau and V. A. Drits, *Am. Mineral.*, 1997, **82**, 962–978.
55 X. Qian, L. Chen, L. Yin, Z. Liu, S. Pei, F. Li, G. Hou, S. Chen, L. Song, K. H. Thebo, H.-M. Cheng and W. Ren, *Science*, 2020, **370**, 596–600.
56 Y. Tao, Y. Wei, Y. Liu, J. Wang, W. Qiao, L. Ling and D. Long, *Energy Environ. Sci.*, 2016, **9**, 3230–3239.
57 Y. Zhang, F. Wan, S. Huang, S. Wang, Z. Niu and J. Chen, *Nat. Commun.*, 2020, **11**, 2199.
58 M. Harada, F. Kotegawa and M. Kuwa, *ACS Appl. Energy Mater.*, 2022, **5**, 278–294.
59 Z. Zhong, J. Li, L. Li, X. Xi, Z. Luo, G. Fang, S. Liang and X. Wang, *Energy Storage Mater.*, 2022, **46**, 165–174.
60 D. Zhang, J. Cao, X. Zhang, N. Insin, S. Wang, J. Han, Y. Zhao, J. Qin and Y. Huang, *Adv. Funct. Mater.*, 2021, **31**, 2009412.
61 Y. Liu, Z. Qin, X. Yang and X. Sun, *Adv. Funct. Mater.*, 2022, **32**, 2106994.
62 G. Fang, C. Zhu, M. Chen, J. Zhou, B. Tang, X. Cao, X. Zheng, A. Pan and S. Liang, *Adv. Funct. Mater.*, 2019, **29**, 1808375.
63 Y. Ma, Y. Ma, T. Diemant, K. Cao, X. Liu, U. Kaiser, R. J. Behm, A. Varzi and S. Passerini, *Adv. Energy Mater.*, 2021, **11**, 2100962.
64 Z. Song, L. Miao, L. Ruhlmann, Y. Lv, L. Li, L. Gan and M. Liu, *Angew. Chem., Int. Ed.*, 2023, **62**, e202219136.
65 S. Zheng, D. Shi, D. Yan, Q. Wang, T. Sun, T. Ma, L. Li, D. He, Z. Tao and J. Chen, *Angew. Chem., Int. Ed.*, 2022, **61**, e202117511.
66 P. Oberholzer, E. Tervoort, A. Bouzid, A. Pasquarello and D. Kundu, *ACS Appl. Mater. Interfaces*, 2019, **11**, 674–682.
67 L. Wang, K.-W. Huang, J. Chen and J. Zheng, *Sci. Adv.*, 2019, **5**, eaax4279.
68 B. Ravel and M. Newville, *J. Synchrotron Radiat.*, 2005, **12**, 537–541.
69 K. D. Kwon and G. Sposito, in *Advances in the Environmental Biogeochemistry of Manganese Oxides*, ed. X. Feng, W. Li, M. Zhu and D. L. Sparks, American Chemical Society, Washington, DC, 1st edn, 2015, ch. 4, vol. 1197, pp. 51–64.

